analytica

MDPI

Article

Synthesis and Characterization of Carbon–Alumina Electrodes for Simultaneous Detection of Aclonifen and Methyl Parathion

Tatjana Novaković [1], Tanja Barudžija [2] and Zorica Mojović [1,*]

[1] Department of Catalysis and Chemical Engineering, Institute of Chemistry, Technology and Metallurgy, University of Belgrade, Njegoševa 12, 11000 Belgrade, Serbia; tatjana.novakovic@ihtm.bg.ac.rs
[2] Vinča Institute of Nuclear Sciences—National Institute of RS, University of Belgrade, Mike Petrovića Alasa 12-14, 11000 Belgrade, Serbia; tbarudzija@vin.bg.ac.rs
* Correspondence: zorica.mojovic@ihtm.bg.ac.rs

Abstract

Alumina–based electrodes offer promising possibilities for sensitive electrochemical sensors, but their development is hindered by poor intrinsic electrical conductivity. To overcome this limitation, new carbon-alumina composites were synthesized via a sol-gel method using two distinct calcination approaches: conventional and flash-calcination. The structural and textural properties of pure alumina samples were affected by the calcination approach. The introduction of carbon reduced the crystallite size and increased the specific micropore surface area and total pore volume of the samples. Electrochemical characterization by cyclic voltammetry and electrochemical impedance spectroscopy revealed that the optimal sample was obtained by conventional calcination for 30 min. This approach produced optimal structural integration, with a well-connected network and superior charge-transfer kinetics. The optimized carbon-alumina composite demonstrated excellent performance for the simultaneous electrochemical detection of methyl parathion and aclonifen by utilizing intermediate reduction products. The resulting sensor achieved wide linear ranges (0.5 to 20 μM) alongside low detection limits of 0.08 μM for methyl parathion and 0.14 μM for aclonifen, establishing these composites as effective materials for sensing applications.

Keywords: alumina; carbon; electrochemical detection; aclonifen; methyl parathion

1. Introduction

Global food demand requires the use of chemicals in everyday agriculture, such as artificial fertilizers and pesticides. The beneficial effects of these treatments are well known [1]. However, there is growing concern about their adverse effects on the health of people, animals [2], and plants [3]. Reports show that the accumulation of pesticides is evident all over the world [4–7]. Besides their toxicity, pesticides present an additional problem due to their persistence in the environment [8] and their influence on the human health as endocrine disruptors [9,10].

The tracking of the presence of pesticides and their residues in fresh water, soil, and food is rapidly becoming a need that requires on–site analysis. Reliable techniques for pesticide detection such as chromatographic techniques [11,12], surface-enhanced Raman scattering [13], and enzyme-linked immunosorbent assay [14] require expensive equipment, complicated sample preparation, and well-trained professionals.

Academic Editor: Chiara Zanardi

Received: 20 October 2026
Revised: 1 November 2026
Accepted: 4 November 2026
Published: 4 November 2026

Copyright: © 2026 by the authors. Licensee MDPI, Basel, Switzerland. This article is an open access article distributed under the terms and conditions of the Creative Commons Attribution (CC BY) license.

Electrochemical methods are fast, portable, reliable and very easy to use [15]. To achieve detection limits comparable to well-established techniques, new electrodes are being developed. Metal oxide materials are often employed due to their high surface area, active surface sites and electrical and semiconducting properties [16]. This type of sensor often employs rare earth elements [17,18], or other critical materials, such nickel or cobalt [19].

Alumina, Al_2O_3, is a highly abundant metal oxide that is also non-toxic, preventing secondary pollution from developed sensors. In the past decade, alumina-modified electrodes have attracted research interest. The pioneering work of Zak and Kuwana [20] highlighted that alumina on the electrode surface influences proton-coupled electron transfer reactions. Further investigations by the Compton group [21] corroborated and expanded the original research, providing a better understanding of the electrode processes occurring on alumina-modified surfaces. The researchers examined the influence of the type of alumina, the size of alumina particles, and the type of electrode used on the efficiency of the electrochemical process [22–24]. The advantages of alumina-modified electrodes include improved selectivity, enhanced sensitivity, greater stability, cost–effectiveness, and ease of fabrication [25].

However, the major disadvantage of alumina is its insulating property. The poor electrical conductivity of alumina hinders electron transfer and reduces overall electrode conductivity. Its insulating nature slows charge transfer between the analyte and the electrode surface. This is usually addressed by combining alumina with a conductive material, such as graphite. Previously, carbon–alumina materials have been explored for electrode modifications due to the combination of alumina's adsorptive or catalytic properties and carbon's electrical conductivity. For instance, our group recently utilized alumina as a catalyst for sawdust combustion to yield a biochar–alumina composite [26]. However, such methods often result in heterogeneously distributed phases where the carbon and metal oxide are mechanically combined. To achieve a more homogenous material with intimately integrated conductive pathways, alternative chemical routes are required.

In this work, the simultaneous optimization of structural stability and electrical conductivity was achieved by using sol-gel co-processing to embed conductive carbon black into a porous alumina framework (bottom-up approach). The effect of thermal treatment was investigated by employing two approaches: traditional ramp-heating and flash-calcination. The resulting material was used as an electrochemical sensor for pesticide detection. The novelty of this study lies in the strategic combination of an in–situ carbon black–doped sol–gel route to optimize electrochemical sensing, rather than crystalline phase purity. While traditional processing demands hours of high-temperature calcination to yield isolated phases, we established that a highly responsive sensor matrix can be fabricated at 600 °C within just 30 min of holding time. This approach shows that the structural features and defects of an incomplete amorphous/γ-alumina transition phase, when integrated with an optimized conductive carbon network can be successfully employed in electrochemical detection applications. The carbon-alumina composites were used for simultaneous detection of aclonifen and methyl parathion. While independent electrochemical assays exist for these pesticides, this study successfully addresses the challenge of overlapping reduction peaks, offering a novel sensing platform for their simultaneous quantification.

2. Materials and Methods

2.1. Materials

All reagents were of analytical grade and used without further purification. Sodium hydroxide (NaOH), nitric acid (HNO_3), sulfuric acid (H_2SO_4), boric acid (H_3BO_3), glacial acetic acid (CH_3COOH), phosphoric acid (H_3PO_4) lead nitrate ($Pb(NO_3)_2$), aluminium

https://doi.org/10.3390/analytica7040094

nitrate ($Al(NO_3)_3$), iron(II) chloride ($FeCl_2$), potassium chloride (KCl) were purchased from Merck (Darmstadt, Germany). Aluminum isopropoxide, potassium ferricyanide ($K_3[Fe(CN)_6]\cdot 3\ H_2O$), potassium ferrocyanide ($K_4[Fe(CN)_6]\cdot 3\ H_2O$), aclonifen (A) and methyl parathion (MP) were purchased from Sigma-Aldrich (St. Louis, MO, USA). Carbon black (Vulcan XC72R) was purchased from Cabot Corp., Boston, Massachusetts AR, USA).

2.2. Synthesis of Carbon/Alumina Composites

The carbon–alumina composites were synthesized by adding carbon black to boehmite sol, followed by drying and calcination.

The synthesis involved mixing the planned amounts of carbon with boehmite sol, as a source of alumina. Boehmite sol was prepared by the hydrolysis of aluminum isopropoxide according to the procedure given by Yoldas [27]. To prepare the boehmite sol, aluminum isopropoxide was hydrolyzed in excess amount of water (100:1 H_2O-Al^{3+}, mol) at 80 °C, followed by peptization with an appropriate amount of HNO_3 (0.07:1 H^+/Al^{3+}, mol) to form a stable colloidal sol. The sol was kept at a constant temperature for the desired time under reflux conditions, during which most of the alcohol was evaporated. Five samples with 10 mass% carbon relative to boehmite were synthesized. After drying at 40 °C for 24 h and at 110 °C for 24 h, two thermal regimes were applied. In the first, three samples were heated at 2 °C min^{-1} until a temperature of 600 °C was reached and then held at that temperature for 10 min (sample CA10), 20 min (sample CA20) and 30 min (sample CA30). Alumina samples without carbon black were synthesized in the same manner and labelled as A10, A20 and A30. The second thermal treatment involved introducing a sample mass of 3 g of powder from room temperature into an already preheated oven at 600 °C for a dwell duration of 1 min (sample CAF1) and 2 min (sample CAF2), under a stagnant air atmosphere. After a dwell duration samples were immediately removed and allowed to cool to room temperature in ambient air. This procedure established a shock-heating thermal history (flash calcination). The samples without carbon black were synthesized in the same manner and labeled as AF1 and AF2.

2.3. Characterization

The X–ray powder diffraction (XRPD) patterns of the investigated samples were recorded using a Rigaku SmartLab diffractometer toperating with Bragg-Brentano focusing geometry, and an X–ray tube with a copper anticathode (CuKα radiation, wavelength 0.154178 nm). The X-ray tube voltage was 40 kV, and the current was 30 mA. Diffraction data were collected between 5° and 80° 2θ, with an angular step of 0.02° and a scanning rate of 2 °min^{-1}.

The textural properties of the synthesized materials were evaluated using low–temperature nitrogen adsorption-desorption isotherms. Nitrogen physisorption measurements were conducted at 77 K using an Autosorb 6300 High-Vacuum Sorption Analyzer (XR high-resolution model) (Anton Paar GmbH, Graz, Austria). Sample preparation involved degassing at the designated preparation port for 2 h at room temperature, followed by a further 16 h at 40 °C, both performed at a residual pressure of <0.1 mPa. The Brunauer–Emmett–Teller (BET) method [28] was applied to determine the specific surface area (S_{BET}) and constant (C_{BET}), following the recommendations of Rouquerol [29], while the specific micropore surface area ($S_{DRmicro}$) was determined by the Dubinin–Radushkevich method [30]. The Dubinin–Radushkevich method and the Barrett, Joyner, and Halenda (BJH) method [31] were used to evaluate pore size distribution. All textural data were processed using the Kaomi software package, version 2.03 (Anton Paar GmbH, Graz, Austria).

2.4. Electrochemical Measurement

Electrochemical measurements were performed in a three-electrode cell using an Autolab electrochemical workstation (PGSTAT302N, Metrohm–Autolab BV, Utrecht, The Netherlands) with an Ag/AgCl electrode (in 3 M KCl) as the reference electrode and a platinum rod as the counter electrode. The working electrode consisted of a hollow Teflon tube (1 mm diameter) packed with modified carbon paste, with electrical contact established using a copper wire. The modified carbon paste was prepared by manually mixing 1 g of sample with 0.2 g of carbon black (CB, Vulcan XC-72R) (sample/carbon black ratio 5/1) and 0.4 mL of paraffin oil. Electrochemical characterization of samples was carried out in 5 mM $[Fe(CN)_6]^{3-/4-}$ in 0.1 M KCl as the supporting electrolyte using cyclic voltammetry (CV) at scan rates ranging from 20 to 200 mV s^{-1} and electrochemical impedance spectroscopy (EIS) at the open-circuit potential (OCP) with a 5 mV rms sinusoidal perturbation over the frequency range 10 kHz to 10 mHz. The electrochemical behavior toward aclonifen and methyl parathion was examined in Britton–Robinson (BR) buffer solutions over the pH range 5–8 using CV at a scan rate of 50 mV s^{-1}. Square wave voltammetry (SWV) was employed to investigate the dependence of the electrode response on analyte concentration, and the optimized parameters were determined for both aclonifen and methyl parathion. The optimized parameters for simultaneous electrochemical sensing of MP ands A by SWV were: accumulation potential −1 V vs. Ag/AgCl, pulse amplitude 0.04 V and accumulation time 15 s. Stock solutions of aclonifen and methyl parathion were prepared by dissolving an appropriate amount of pesticide in ethanol to obtain a concentration of 10 mM.

3. Results

3.1. XRPD Structure Analysis

The XRPD patterns of the alumina and carbon-alumina samples were recorded in the 2θ range from 5 to 80° (Figure 1).

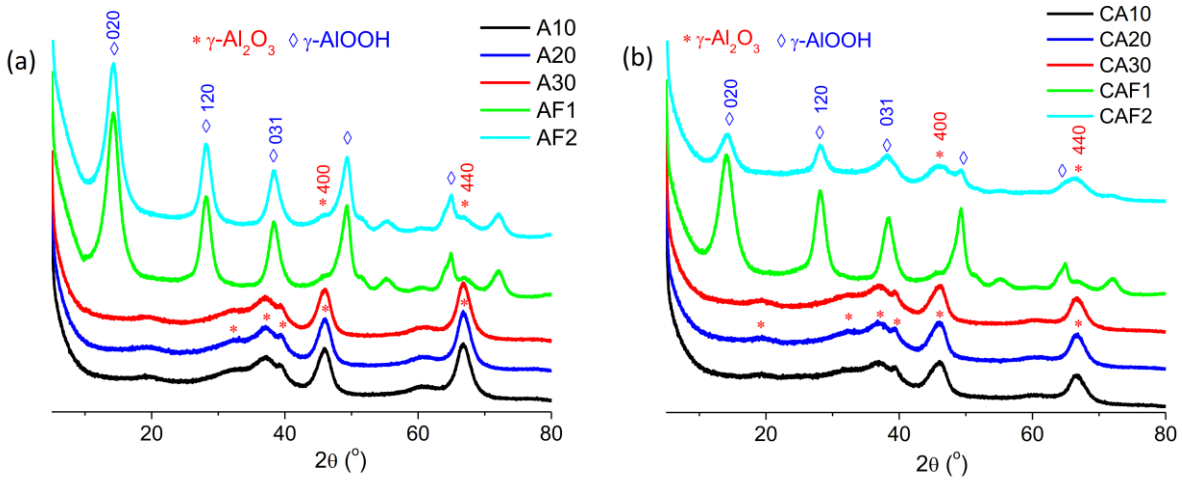


Figure 1. X-ray powder diffractions (XRPD) patterns of (**a**) pure alumina samples and (**b**) carbon–alumina samples.

Reflection peaks corresponding to the γ-AlOOH structure are present in the samples obtained by flash calcination (JCPDS card 01-072-0359(A)). Reflection peaks corresponding to γ-Al_2O_3 are present in the samples obtained by conventional calcination (JCPDS card 01-079-1558(C)), although some low-intensity reflections can also be observed in the

XRD patterns of the flash-calcined samples. The peak intensities are higher in the pure alumina samples than in their carbon-containing counterparts.

The crystallite sizes (D) of the synthesized alumina and carbon-containing composite samples, were calculated using the Debye–Scherrer formula:

$$D = \frac{K\lambda}{\beta cos\theta} \quad (1)$$

where K is the shape factor (0.9), λ is the wavelength of the X-ray used (0.154178 nm), β is the full width at half maximum (FWHM) of the diffraction peak (in radians), and θ is the Bragg angle (the angle of diffraction in radians).

The calculated crystallite sizes are presented in Table 1.

Table 1. Calculated crystallite size values obtained from XRPD analysis.

Sample		A10	A20	A30	AF1	AF2	CA10	CA20	CA30	CAF1	CAF2
		Crystallite Size (nm)									
	d400	3.9	4.1	4.0			3.0	3.4	3.4		
	d440	4.3	4.5	4.5			3.9	4.2	4.2		
plane	d020				3.9	3.9				3.4	3.8
	d120				5.1	5.1				4.9	5.1
	d031				4.9	4.7				4.5	3.7

Pure alumina samples (series A) obtained by conventional calcination show a mild increase in crystallite size as the calcination time extends from 10 to 20 min, after which the size stabilizes. This indicates that the rapid growth phase of the γ-alumina lattice under static thermal conditions occurs within the first 20 min at 600 °C.

The incorporation of carbon black into the sol–gel matrix (CA series) leads to the development of smaller crystallite sizes. This indicates that dispersed carbon black particles act as physical barriers that restrict mass transport and limit the long-range diffusion of aluminum and oxygen ions required for crystal growth during calcination.

Pure alumina samples obtained by flash calcination (AF samples) show that extending the time from 1 to 2 min has almost no effect on the crystallite size. However, when carbon black is introduced into the flash-calcined configuration (CAF samples) the inhibition of crystallite growth becomes further pronounced, particularly along the d020 and d031 planes. The structural obstacles created by the carbon black matrix limit the rapid structural reorganization triggered by flash calcination.

The growth restriction observed due to the presence of carbon black in both calcination methods aligns with similar findings regarding alumina synthesis in the presence of a carbonaceous phase [32].

The peak intensities are higher in the pure alumina samples than in their carbon-containing counterparts. There are two factors that can cause this reduction in diffraction peak intensity for carbon-alumina samples. The first is the "dilution effect", i.e., the presence of amorphous carbon black in the network lowers the overall volume fraction of the crystalline alumina phase in the composite matrix. Secondly, the lower peak intensity is accompanied by peak broadening, which is a direct consequence of the smaller crystallite sizes in the carbon-containing samples.

3.2. Textural Properties

Nitrogen adsorption–desorption isotherms of alumina and carbon–alumina samples are presented in Figure 2a,b, and differential pore size distribution curves are presented in Figure 2c,d. All investigated samples exhibit Type IVa isotherms accompanied by H2-type hysteresis loops. The initial part of this type of isotherm is similar to a Type II isotherm, while at high relative pressure it shows a saturation plateau of varying length. The

pore structure of materials showing this type of isotherm and H2-type hysteresis loop is complex and tends to consist of mesoporous frameworks containing disordered, interconnected networks of pores of different size and shape [27].

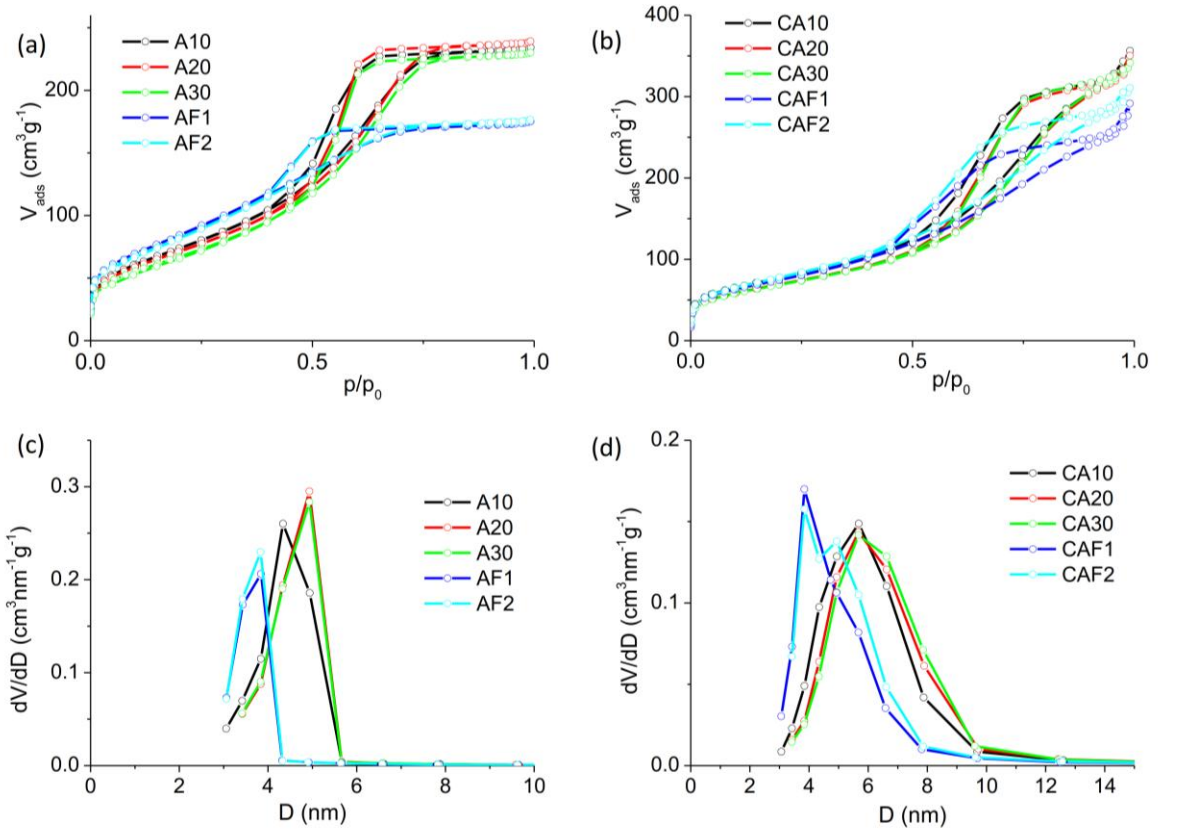


Figure 2. Low-temperature nitrogen adsorption-desorption isotherms for (**a**) pure alumina samples and (**b**) carbon–alumina samples, and differential pore size distribution curves for (**c**) pure alumina samples and (**d**) carbon–alumina samples.

The textural properties of the synthesized materials were evaluated using low-temperature nitrogen adsorption–desorption isotherms, and the corresponding parameters are presented in Table 2.

The results in Table 2 show that for the conventionally calcined pure alumina samples (series A), extending the heating time from 10 to 30 min induces a gradual decrease in the specific surface area (S_{BET} from 273 to 249 m^2g^{-1}), along with a minor drop in the micropore contribution ($S_{DRmicro}$). This trend directly corresponds to the thermal stabilization and growth of the gamma-alumina crystallites previously evidenced by XRPD. In contrast, the flash-calcined samples (AF1 and AF2) retain higher surface areas due to the ultra-short exposure time, which effectively halts extensive lattice coarsening but leaves the total pore volume restricted (V_p approx. 0.27 cm^3g^{-1}).

Table 2. Textural properties of samples based on low-temperature nitrogen adsorption–desorption isotherm analysis.

Sample	S_{BET} (m^2g^{-1})	C_{BET}	$S_{DRmicro}$ (m^2g^{-1})	V_p (cm^3g^{-1})	D_{BJH} (nm)	D_{DR} (nm)
A10	273	59.3	49	0.362	4.3	1.7
A20	263	61.1	43	0.370	4.9	1.7
A30	249	58.4	41	0.356	4.9	1.7

AF1	317	45.9	75	0.270	3.8	1.9
AF2	314	40.7	69	0.273	3.8	1.9
CA10	280	92.7	66	0.535	5.7	1.7
CA20	251	92.6	68	0.520	5.7	1.8
CA30	249	91.9	66	0.520	5.7	1.8
CAF1	270	93.7	73	0.429	3.8	2.2
CAF2	284	73.6	71	0.473	3.8; 4.9	1.9

The incorporation of carbon black produces distinct changes in the porous architecture. In the conventionally calcined composite series (CA10, CA20, and CA30), introduction of the carbon phase causes a significant increase in $S_{DRmicro}$ (up to 68) and in the total pore volume (Vp increases up to 0.535 cm^3g^{-1}) and yields wider pore size distributions with a shift of the predominant pore diameter to larger values (D_{BJH} = 5.7 nm). This expansion confirms that well-dispersed carbon black acts as a structural spacer, creating high interparticle mesoporosity and preventing dense sintering of the alumina matrix. Furthermore, the carbon-containing composites show an increase in the C_{BET} constant (rising from approx. 59 to approx. 93), corroborating the increase in micropore content [33] as well as the enhanced surface affinity [34] introduced by the carbonaceous surface sites.

3.3. Electrochemistry

3.3.1. Electrochemical Characterization

The initial assessment of the investigated electrode surface and electron-transfer kinetics was obtained from the electrode response toward the ferro/ferricyanide redox couple. Cyclic voltammograms recorded at 50 mVs^{-1} are presented in Figure 3a for the samples calcined for various times and in Figure 3b for the samples flash-calcined for various times. The characteristic pair of peaks corresponding to the oxidation and reduction of the $[Fe(CN)_6]^{3-/4-}$ redox couple can be seen in all recorded voltammograms. For both groups of samples, the increase in current response with increasing of calcination time is evident. The pure alumina electrode exhibited an extremely wide peak-to-peak separation, typical of highly resistive, insulating materials. The introduction of a carbon phase during synthesis improved the charge-transfer kinetics in both series, although the improvement was more pronounced for the conventionally calcined samples.

Further investigation of the carbon–alumina samples was performed at various scan rates (CVs are presented in Figures S1a–S5a in the Supplementary Materials). Plots of peak current against the square root of scan rate (Figures S1b–S5b) showed a linear relationship, indicating a diffusion-controlled process.

Peak-to-peak separation values of up to 250 mV were obtained for conventionally calcined samples, showing that the kinetics were quasi-reversible, while values of up to 550 mV obtained for flash-calcined samples showed that the electron transfer followed irreversible kinetics.

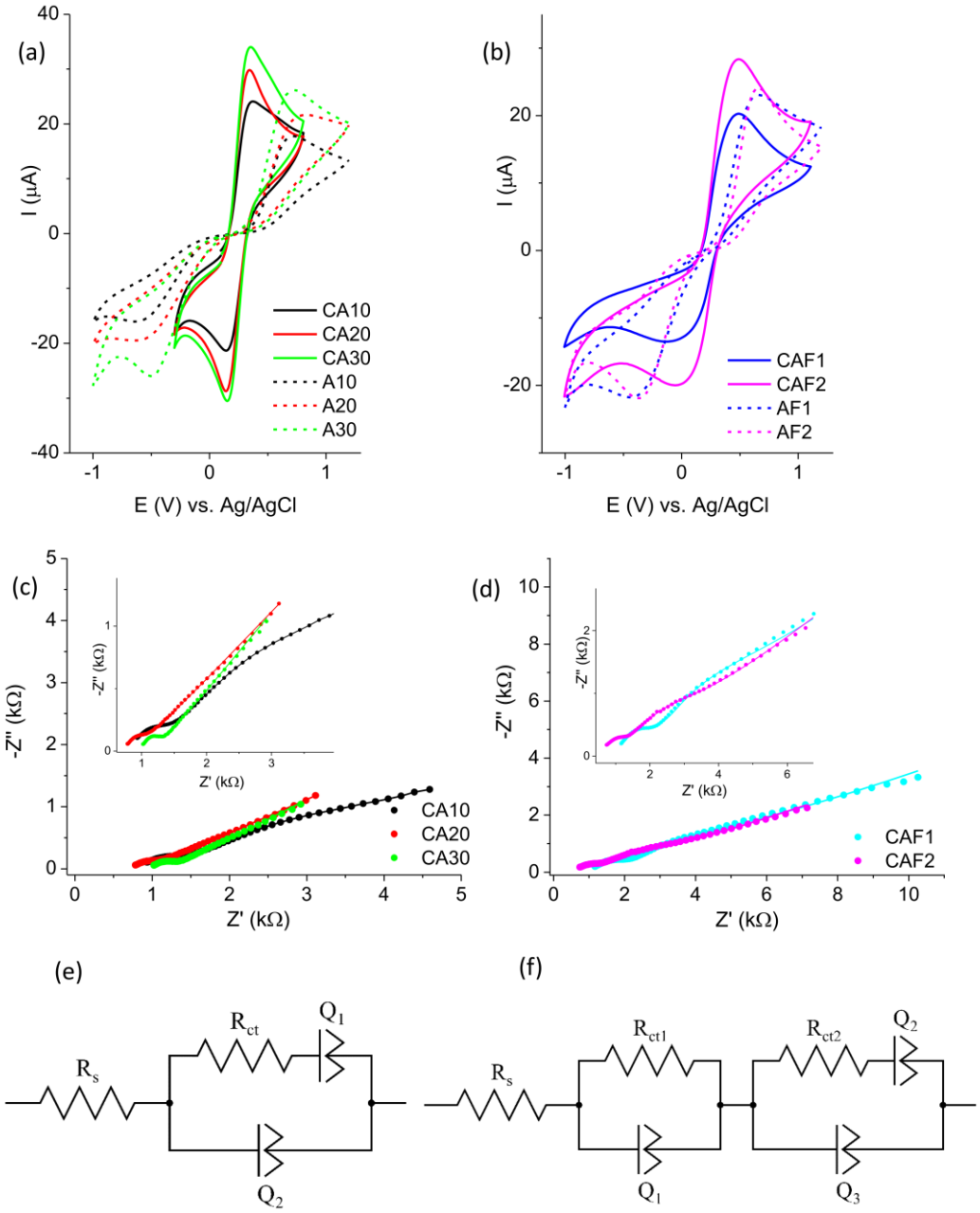


Figure 3. (**a**) Cyclic voltammograms of modified carbon paste electrodes recorded at a scan rate of 50 mVs^{-1} for (**a**) conventionally calcined alumina samples and (**b**) flash-calcined alumina samples. Nyquist plots for (**c**) conventionally calcined carbon–alumina samples and (**d**) flash-calcined carbon–alumina samples. The electrolyte was 5 mM $[Fe(CN)_6]^{3-/4-}$ in 0.1 M KCl. The inset figures in c and d represent enlarged section of the Nyquist plots. The equivalent electric circuits used to fit the EIS data: (**e**) circuit A and (**f**) circuit B.

The electrochemical heterogeneous standard rate constant (k^0) for a quasi-reversible process can be calculated using the modification of the Nicholson procedure [35] by Lavagnini et al. [36] which extends the application of the Nicholson procedure to $n \cdot \Delta Ep > 200$ mV by calculating Ψ from ΔEp:

$$\Psi = \frac{-0.6288+0.0021X}{1-0.017X} \quad (2)$$

where $X = \Delta Ep$, and

$$\psi = k^0 \left[\frac{\pi D n v F}{RT}\right]^{-\frac{1}{2}} \quad (3)$$

The values of k^0 can be obtained as the slope of Ψ versus $[\pi DnF/RT]^{-1/2}v^{-1/2}$. These plots for calcined samples are presented in Figures S1c–S3c in the Supplementary Materials.

On the other hand, the value of k^0 for an irreversible process can be determined using the equation [37]:

$$E_{pa} = E^0 + \frac{RT}{(1-\alpha)nF}\left[0.78 + ln\frac{\sqrt{D}}{k^0} + ln\sqrt{\frac{(1-\alpha)nFv}{RT}}\right] \quad (4)$$

where R, T and F are the universal gas constant, absolute temperature and Faraday constant, respectively, D is the diffusion coefficient of the reduced species, k^0 is the heterogeneous standard rate constant, α is the charge-transfer coefficient and n is the number of electrons transferred during the heterogeneous reaction.

The plots of Ep versus lnv for flash-calcined samples are presented in Figures S4c and S5c in the Supplementary Materials. The values of the heterogeneous charge-transfer rate constant, k^0 were 6.6×10^{-4} cm s^{-1}, 9.4×10^{-4} cm s^{-1}, 9.9×10^{-4} cm s^{-1}, 1.1×10^{-5} cm s^{-1} and 1.6×10^{-5} cm s^{-1} for CA10, CA20, CA30, CAF1 and CAF2, respectively. The value of the diffusion coefficient of potassium ferrocyanide (6.5×10^{-6} cm^2 s^{-1}) was obtained from literature data [23].

Electrochemical impedance spectroscopy was employed to investigate the different resistive and capacitive processes that contribute to the overall electrode behavior. Recorded Nyquist plots are presented in Figure 3c,d. The Nyquist plots of CA20 and CA30 electrodes consisted of one semicircle and a linear part at lower frequencies, while the Nyquist plots of CA10, CAF1 and CAF2 consisted of two semicircles and a linear part at lower frequencies. The difference in electrode response is more obvious in the Bode plot (Figure S6 in the Supplementary Materials), where two relaxation time constants are visible for the latter three electrodes. Hence, the spectra of CA20 and CA30 were fitted with an equivalent circuit consisting of the series combination of an internal resistance Rs, and a parallel combination of a serial connection Rct1–CPE1 with CPE2 (equivalent circuit A, Figure 3e), while the spectra of CA10, CAF1 and CAF2 were fitted with an equivalent circuit consisting of the series combination of an internal resistance Rs, a parallel Rct1‖CPE1 and a parallel Rct2‖CPE2 (equivalent circuit B, Figure 3f). The results of the fit obtained using these equivalent circuits are presented in Table 3.

Table 3. Parameters obtained from fitting the Nyquist plots.

Electrode	Rs (Ω)	R_{ct} (Ω)	Y_1 (μSs^{n1})	n1	Y_2 (nSs^{n2})	n2	χ^2			
CA20	730	250	467	0.3	5.8	0.6	0.005			
CA30	980	270	591	0.4	4.9	0.7	0.006			
	Rs (Ω)	**R_{ct1} (kΩ)**	**Y_1 (μSs^{n1})**	**n1**	**R_{ct2} (Ω)**	**Y_2 (μSs^{n1})**	**n2**	**Y_3 (μSs^{n1})**	**n3**	**χ^2**
CA10	810	1.17	278	0.6	614	474	0.3	7.8	0.5	0.003
CAF1	850	1.92	6.0	0.5	86	3.8	0.9	135	0.3	0.009
CAF2	420	1.50	9.9	0.4	82	3.1	0.9	197	0.3	0.005

In this configuration, the high-frequency response for CA10, CAF1, and CAF2 is governed by the Rct1‖CPE1 elements, which represent the charge-transfer resistance and geometric capacitance at the internal micro-interfaces between the poorly consolidated modifier phases and the host carbon black paste matrix. The low-frequency peaks for these electrodes are described by the Rct2‖CPE2 sub-circuit, corresponding to the true interfacial Faradaic charge-transfer kinetics of the redox probe at the outer electrode/electrolyte boundary. The shift of both time constants to higher frequencies in the flash-calcined samples (CAF1 and CAF2) indicates accelerated electron-transfer kinetics. The ultra-short thermal shock restricts crystallite growth, yielding highly confined alumina domains that enable short-range electronic relaxation across individual micro-interfaces. However,

these flash-calcined domains are poorly consolidated and therefore form an electrically restricted network across the bulk paste. By contrast, the prolonged calcination time for the conventionally calcined samples CA20 and CA30 enables structural integration and causes the dual-peak profile to collapse into a single relaxation peak.

3.3.2. Electroanalytical Properties

The electroanalytical properties of the carbon–alumina electrodes were investigated through their response to aclonifen and methyl parathion. Aclonifen, an herbicide, and methyl parathion, an insecticide, are widely used in agriculture. Both compounds are xenobiotics due to their persistence and potential bioaccumulation in the environment, posing ecotoxicological risks to non-target organisms and contributing to soil and water contamination. Sensitive and selective detection of these xenobiotic substances is of great importance for effective monitoring, environmental protection, and timely implementation of control and remediation measures. Aclonifen is in active use, and is officially designated as a Priority Substance (i.e., it must be legally monitored) under the European Water Framework Directive (WFD) [38]. Methyl parathion is being banned worldwide. Nevertheless, due to its efficiency and low cost, MP is still used illegally [39].

The initial response of carbon–alumina-based electrodes toward nitro-pesticides was tested in 0.1 M BR buffer at pH 7 containing 100 μM aclonifen. The CVs were compared with those recorded in buffer without aclonifen to identify the response originating from aclonifen (Figure 4). The initial scan was in the cathodic direction, followed by the anodic direction.

The CV recorded in pure buffer showed a cathodic peak characteristic of specific surface groups of the investigated composite material. The CV of conventionally calcined sample-based electrodes showed a peak at potentials around −0.5 V, which can be correlated with the reduction of alumina surface groups [26], while the CV of flash-calcined sample-based electrodes showed a peak at a more negative value (−1.1 V). This peak can be assigned to the reduction of oxygen-containing functionalities [40], indicating that the response of flash-calcined samples is dominated by carbon black. A shift in peak position can be seen with variation in electrode composition when the carbon black content in the carbon paste electrode is increased (more detail in Supplementary Materials, Figure S7), confirming the assignment of the peaks. The CV recorded in the presence of aclonifen was characterized by an additional cathodic peak at a potential around −0.9 V and an anodic peak at potentials around 0.3 V. the cathodic peak originated from reduction of the nitro group of aclonifen, while the anodic peak originated from oxidation of the intermediate formed during this reduction [41].

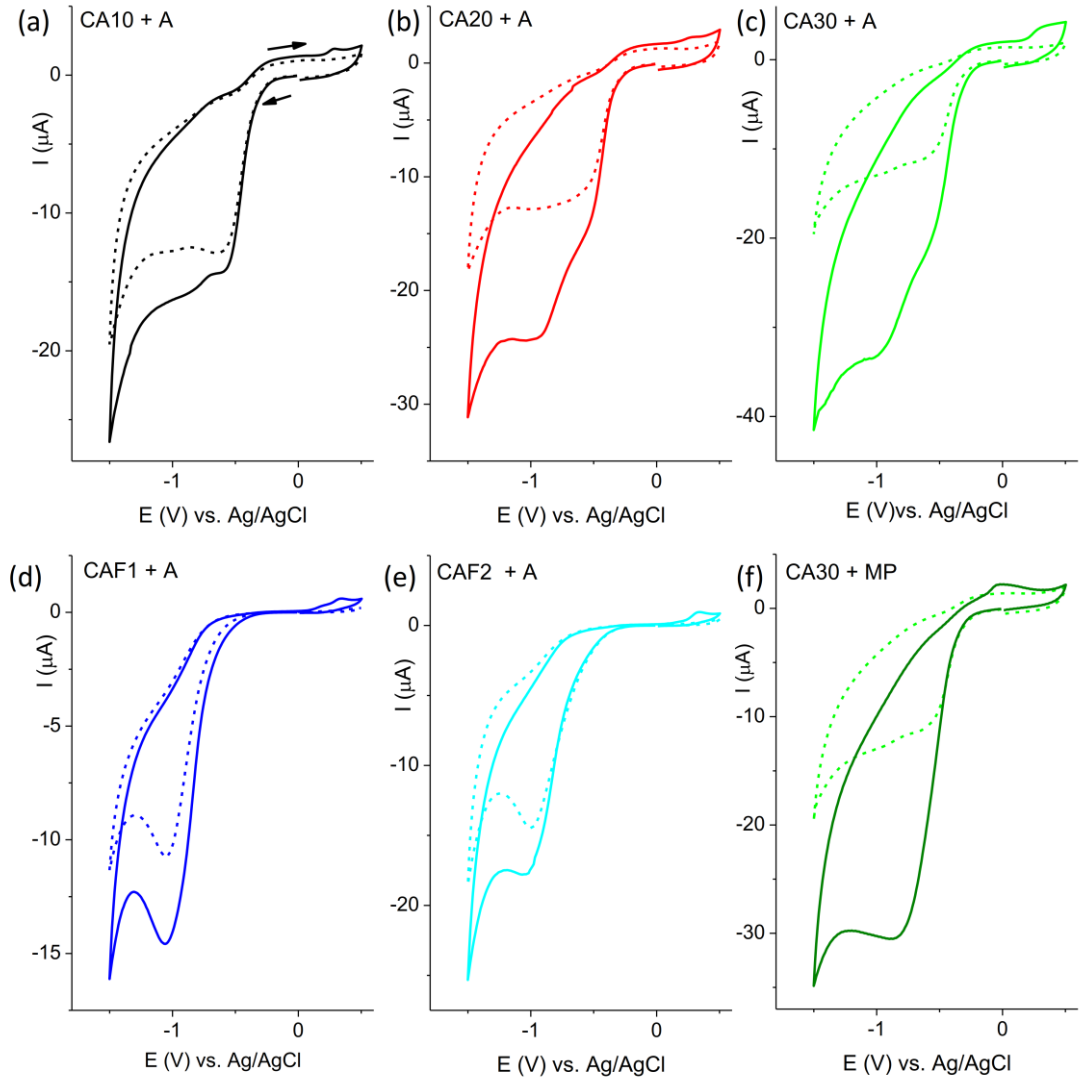


Figure 4. (**a**–**e**) CV recorded on the investigated carbon–alumina electrodes in 0.1 M Britton–Robinson buffer, pH 7, without (dashed line) and with 100 μM aclonifen (solid line); (**f**) CV recorded at the CA30 electrode in 0.1 M BR buffer, pH 7, without (dashed line) and with 100 μM methyl parathion (solid line); scan rate 50 mVs^{-1}. The arrows in (**a**) indicate the scan direction applied for all presented CVs.

The CV of the CA30 electrode recorded in methyl parathion-containing buffer is shown in Figure 4f. The peak for MP reduction can be seen at around −0.8 V, while the peak for intermediate oxidation is observed at around 0 V. The reduction peak potentials of MP and A overlap. However, simultaneous detection of MP and A is possible based on oxidation of the formed intermediates. The peak separation of the intermediated is approximately 300 mV, enabling reliable simultaneous detection. Verification of the carbon–alumina composite contribution to the electrode response was obtained by recording the cyclic voltammogram of a carbon paste electrode prepared without carbon–alumina (Figure S8). The anodic peak of intermediate oxidation appears, but the currents are very low. Further analysis of the electrode response was performed only for the anodic peak.

The response of carbon–alumina based electrodes toward aclonifen was tested in the pH range 5–8 (Figure 5a–e).

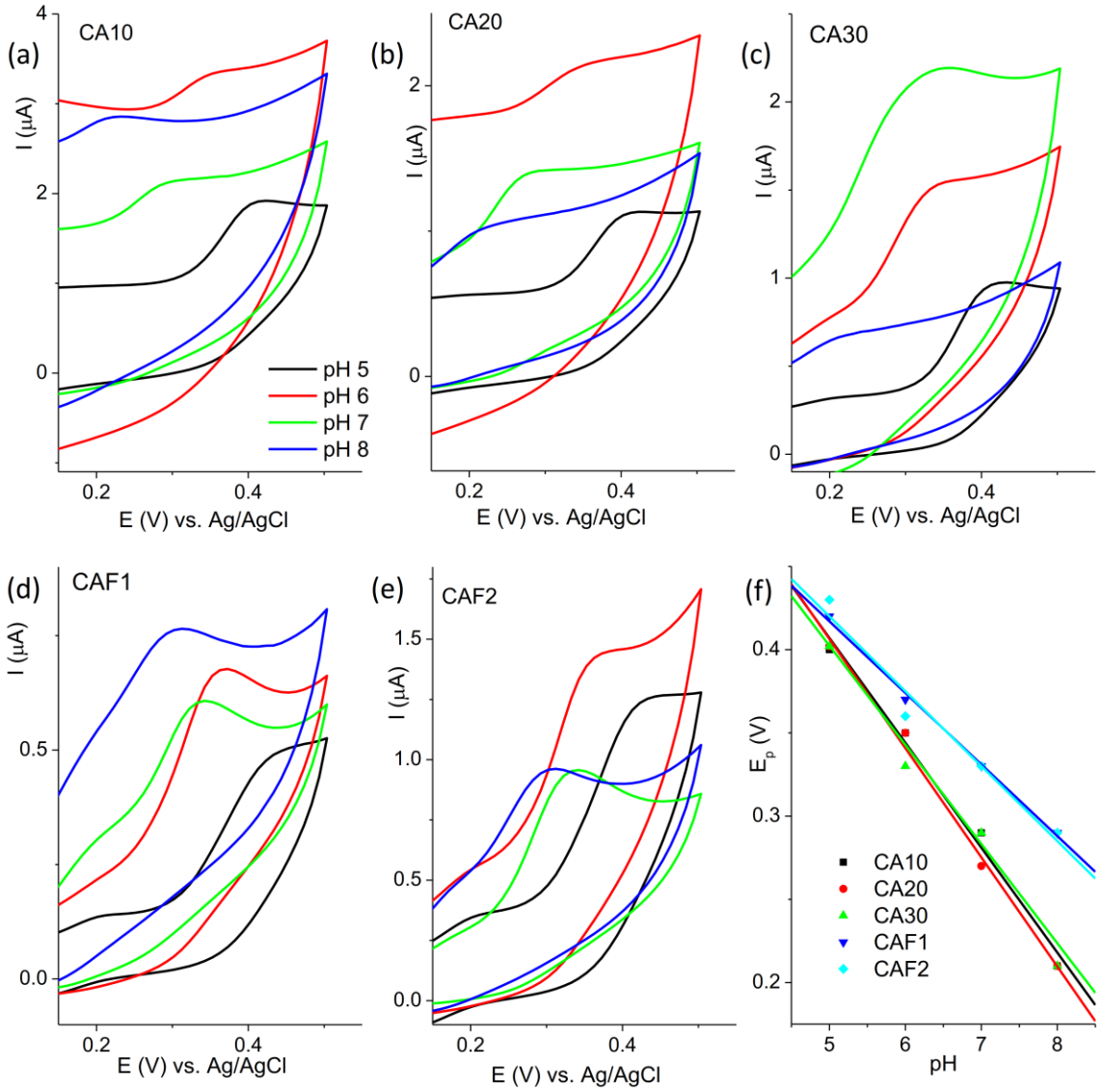


Figure 5. CV recorded at 50 mV s^{-1} in 0.1 M BR buffer containing 100 μM aclonifen at pH 5–8 at (**a**) CA10; (**b**) CA20; (**c**) CA30; (**d**) CAF1 and (**e**) CAF2 electrodes; (**f**) plot of the dependence of peak potential on pH for all electrodes.

The dependence of the anodic peak potential on pH is shown in Figure 5f. The slope obtained for all conventionally calcined samples was approximately 59 mV pH^{-1}, as expected for a process involving the same number of protons and electrons. The flash-calcined samples showed slopes of approximately 45 mV pH^{-1}, probably due to the influence of sluggish electrode kinetics, i.e., the slope is modified by the transfer coefficient (α).

The CA30 electrode was selected for further investigations, based on its best response toward aclonifen and the charge transfer rate determined in electrochemical characterization. Parallel comparative trials across the entire investigated pH range, as well as repeated trials at pH 7, also confirmed that the CA30 electrode consistently demonstrates the highest response. The dependence of the methyl parathion intermediate anodic peak (at around 0 V) on pH was investigated for the CA30 electrode in the pH range 5–8 (Figure S9a) and the slope was 53 mV pH^{-1} (Figure S9b).

The simultaneous detection of A and MP was performed using square-wave voltammetry. The SWV parameters were optimized before determination of the calibration curve

(Figure S10). The SWV recorded under optimized conditions is presented in Figure 6a, and the calibration plot is shown in Figure 6b.

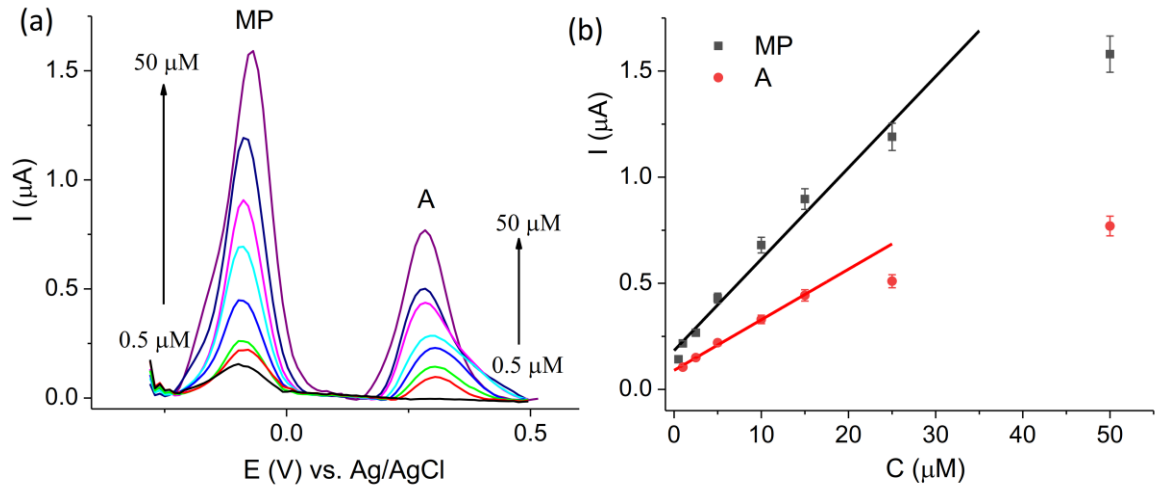


Figure 6. (**a**) SWV recorded in an equimolar concentration of methyl parathion and aclonifen in the range 0.5–50 µM in 0.1 M BR buffer at pH 7; (**b**) calibration curve. Error bars represent the standard error of n = 3 independent replicates.

The calibration curve showed a linear relationship between the current and the MP concentration in the range 0.5–25 µM, with the linear regression equation: Ip (µA) = (0.18 ± 0.03) + (0.043 ± 0.003)*C [MP](µM), R^2 = 0.987. A linear relationship between the current and the A concentration was obtained in the concentration range 0.5–20 µM, with the linear regression equation: Ip (µA) = (0.090 ± 0.006) + (0.0238 ± 0.0007)*C [A](µM), R^2 = 0.997.

The estimated limit of detection (LOD) was 0.08 µA and 0.14 µM for MP and A, respectively (signal-to-noise ratio = 3). The reproducibility of the CA30 electrode response was determined by measuring the current response recorded in BR buffer at pH 7 containing an equimolar concentration (10 µM) of A and MP. The relative standard deviation (RSD %) for five independently prepared electrodes was 5.4% and 5.7% for MP and A, respectively. The repeatability of one CA30 electrode was determined over five successive measurements, and the RSD was 3.8% and 5.3% for MP and A, respectively.

Table 4 compares the analytical parameters of the CA30 electrode with other electrodes reported in the literature for MP and A determination.

Table 4. Comparison of analytical parameters of various working electrodes for MP and A detection.

Working Electrode	Method	Analyte	LOD (µM)	Linear Range (µM)	Ref
MWCNT/zirconia	DPV	MP	0.009	19.9–176.8	[42]
EMBPC@CeO_2/GCE	DPV	MP	0.009028	0.01–10	[43]
CeO_2-CuO/rGO (1:1)/GCE	DPV	MP	0.0018	0.0038–0.038, 0.038–0.152	[44]
HCP5@AuNPs–ERGO	DPV	MP	0.001	0.005–30	[45]
PNIPAM/PANI-Cu	DPV	A	0.009	0.01–10, 18–76	[46]
$GdNbO_4$	DPV	A	0.00115	0.02–78	[47]
g-C_3N_4 modified GCE	SWV	A	0.00128	0.01–1.2	[48]
CA30	SWV	MP A	0.08 0.14	0.5–25 0.5–20	This work

A key advantage of the CA30 electrode is its ability to simultaneously detect MP and A with similar sensitivity across a wide concentration range. Despite a higher limit of detection compared with existing alternatives, the inherent versatility of carbon–alumina-based materials offers extensive opportunities for performance enhancement in future studies.

The influence of interfering species on the response of the CA30 electrode toward MP and A was studied at an equimolar concentration of 2.5 μM. A tolerance level of 5% was achieved for Al^{3+}, Pb^{2+}, Fe^{2+}, Cl^{-}, NO_3^{-}, and SO_4^{2-} at concentrations 50 times higher than those of MP and A, whereas the same tolerance level was achieved for 4-nitrophenol, 2-nitrophenol, and Cu^{2+} at concentrations 2 times higher.

The commercially available pesticide formulation containing 600 g/L of aclonifen was used as the sample for evaluating sensor performance. The pesticide was diluted as required, and an appropriate aliquot was added to the buffer solution. Recovery testing was performed using the standard addition method, and the corresponding results are presented in Table 5.

Table 5. Recovery test for aclonifen in real sample.

Sample	Initial Added, μM	Spiked, μM	Found, μM	Recovery, % (n = 3)
Commercial pesticide	4.0	0	3.9	97.5
	4.0	2.0	6.4	106
	4.0	4.0	7.6	95

4. Conclusions

Alumina-based electrodes offer possibilities for the development of sensitive electrochemical sensors. The intrinsic problem with alumina is its poor electrical conductivity. In this work, new carbon–alumina composites are synthesized to overcome this problem. Alumina composites (series A) and carbon–alumina composites (series CA) are synthesized from sol–gel using two calcination methods: conventional calcination and flash calcination. XRPD analysis showed, for both series of samples, that conventional calcination produced the γ-Al_2O_3 phase, while flash calcination produced predominantly the γ-AlOOH phase with some γ-Al_2O_3. The introduction of carbon into the sol–gel matrices resulted in smaller crystallite sizes.

Flash-calcined samples retained higher surface areas than conventionally calcined samples due to the short exposure times. Carbon-containing samples had higher specific micropore surface areas, higher total pore volumes, and wider pore size distributions than pure alumina counterparts.

Electrochemical characterization showed that carbon–alumina samples had better charge transfer kinetics than pure alumina samples. Flash-calcined samples had confined alumina domains enabling fast charge transfer; however, these domains were insulated, resulting in poorly conducting network. By contrast, conventionally calcined samples (at 20 and 30 min) enabled structural integration, producing a well-connected network.

The chosen carbon–alumina composite showed good performance for the simultaneous detection of methyl parathion and aclonifen, using intermediate products formed during the reduction of the major compounds. The sensor showed a linear relationship in the concentration range 0.5–20 μM with limit of detection of 0.08 μM for methyl parathion and 0.14 μM for aclonifen.

Supplementary Materials: The following supporting information can be downloaded at https://www.mdpi.com/article/10.3390/analytica7040094/s1.

Author Contributions: Conceptualization, Z.M.; methodology, Z.M.; investigation, T.N., T.B. and Z.M.; writing—original draft preparation, Z.M.; writing—review and editing, T.N., T.B. and Z.M. All authors have read and agreed to the published version of the manuscript.

Funding: This research has been financially supported by the Ministry of Science, Technological Development and Innovation of the Republic of Serbia (Contract No. 451-03-33/2026-03/200026 and 451-03-33/2026-03/200017). This work is correlated with following UN Sustainable Development Goals: SDS 3, SDG 6, SDG 9, SDG 12 and SDG 13.

Data Availability Statement: The original contributions presented in the study are included in the article and Supplementary Material, and further inquiries can be directed to the corresponding author.

Conflicts of Interest: The authors declare no conflicts of interest.

Abbreviations

The following abbreviations are used in this manuscript:

A	Aclonifen
MP	Methyl parathion
XRPD	X–ray powder diffraction
BET	Brunauer–Emmett–Teller
CV	Cyclic Voltammetry
EIS	Electrochemical Impedance Spectroscopy
OCP	Open-Circuit Potential
BR	Britton–Robinson
SWV	Square Wave Voltammetry

References

1. Cooper, J.; Dobson, H. The benefits of pesticides to mankind and the environment. *Crop Prot.* **2007**, *26*, 1337–1348. https://doi.org/10.1016/j.cropro.2007.03.022.
2. Rohani, F. Pesticides toxicity in fish: Histopathological and hemato-biochemical aspects—A review. *Emerg. Contam.* **2023**, *9*, 100234. https://doi.org/10.1016/j.emcon.2023.100234.
3. Lazarević-Pašti, T.; Milanković, V.; Tasić, T.; Petrović, S.; Leskovac, A. With or Without You?—A Critical Review on Pesticides in Food. *Foods* **2025**, *14*, 1128. https://doi.org/10.3390/foods14071128.
4. Araújo, E.P.; Caldas, E.D.; Oliveira-Filho, E.C. Pesticides in surface freshwater: A critical review. *Environ. Monit. Assess.* **2022**, *194*, 452. https://doi.org/10.1007/s10661-022-10005-y.
5. Duttagupta, S.; Mukherjee, A.; Bhattacharya, A.; Bhattacharya, J. Wide exposure of persistent organic pollutants (PoPs) in natural waters and sediments of the densely populated Western Bengal basin, India. *Sci. Total Environ.* **2020**, *717*, 137187. https://doi.org/10.1016/j.scitotenv.2020.137187.
6. Pistocchi, A.; Dorati, C.; Galimberti, F.; Udias, A.; Bopp, S.; D'Andrimont, R.; Catarino, R.; Schaefer, R.B. A screening study of the spatial distribution and cumulative toxicity of agricultural pesticides in the European Union's waters. *Front Environ. Sci.* **2023**, *11*, 1101316. https://doi.org/10.3389/fenvs.2023.1101316.
7. Huang, Y.; Li, Z. Global mapping of freshwater contamination by pesticides and implications for agriculture and water resource protection. *iScience* **2025**, *28*, 112861. https://doi.org/10.1016/j.isci.2025.112861.
8. Vasseghian, Y.; Hosseinzadeh, S.; Khataee, A.; Dragoi, E.-N. The concentration of persistent organic pollutants in water resources: A global systematic review, meta-analysis and probabilistic risk assessment. *Sci. Total Environ.* **2021**, *796*, 149000. https://doi.org/10.1016/j.scitotenv.2021.149000.
9. Kumar, V.; Sharma, N.; Sharma, P.; Pasrija, R.; Kaur, K.; Umesh, M.; Thazeem, B. Toxicity analysis of endocrine disrupting pesticides on non-target organisms: A critical analysis on toxicity mechanisms. *Toxicol. Appl. Pharmacol.* **2023**, *474*, 116623. https://doi.org/10.1016/j.taap.2023.116623.
10. Pan, J.; Liu, P.; Yu, X.; Zhang, Z.; Liu, J. The adverse role of endocrine disruptingchemicals in the reproductive system. *Front Endocrinol.* **2024**, *14*, 1324993. https://doi.org/10.3389/fendo.2023.1324993.

11. Syrgabek, Y.; Alimzhanova, M. Modern Analytical Methods for the Analysis of Pesticides in Grapes: A Review. *Foods* **2022**, *11*, 1623. https://doi.org/10.3390/foods11111623.
12. Santilio, A.; Girolimetti, S.; Picardo, V. Simple and Rapid High-Performance Liquid Chromatography Method for Simultaneous Determination of Picloram and 2,4-D in Pesticide Formulations. *Analytica* **2022**, *3*, 430–438. https://doi.org/10.3390/analytica3040029.
13. Averkiev, A.; Rodriguez, R.D.; Fatkullin, M.; Lipovka, A.; Yang, B.; Jia, X.; Kanoun, O.; Sheremet, E. Towards solving the reproducibility crisis in surface-enhanced Raman spectroscopy-based pesticide detection. *Sci. Total Environ.* **2024**, *935*, 173262. https://doi.org/10.1016/j.scitotenv.2024.173262.
14. Yue, Y.; Chen, J.; Zhang, M.; Yin, Y.; Dong, Y. Determination of Organophosphorus Pesticides in Vegetables and Fruit by an Indirect Competitive Enzyme-Linked Immunosorbent Assay (ic-ELISA) and a Lateral-Flow Immunochromatographic (LFIC) Strip Assay. *Anal. Lett.* **2022**, *55*, 1701–1718. https://doi.org/10.1080/00032719.2021.2023170.
15. Martins, F.C.O.L.; De Souza, D. New Approaches in Electroanalytical Determination of Triazines-Based Pesticides in Natural Waters. *Analytica* **2023**, *4*, 84–101. https://doi.org/10.3390/analytica4020008.
16. Maheshwaran, S.; Chen, W.-H.; Lin, S.-L.; Ghorbani, M.; Hoang, A.T. Metal oxide-based electrochemical sensors for pesticide detection in water and food samples: A review. *Environ. Sci. Adv.* **2024**, *3*, 154–176. https://doi.org/10.1039/d3va00313b.
17. Ganesan, M.; Devi, R.K.; Liao, A.-H.; Lee, K.-Y.; Gopalakrishnan, G.; Chuang, H.-C. 3D-flower-like porous neodymium molybdate nanostructure for trace level detection of organophosphorus pesticide in food samples. *Food Chem.* **2022**, *396*, 133722. https://doi.org/10.1016/j.foodchem.2022.133722.
18. Thirumalraj, B.; Krishnapandi, A.; Chen, S.-M.; M.S.P., S.; Choe, H. Rational design and interlayer effect of dysprosium-stannate nanoplatelets incorporated graphene oxide: A versatile and competent electrocatalyst for toxic carbamate pesticide detection in vegetables. *ACS Sustain Chem. Eng.* **2020**, *8*, 17882–17892. https://doi.org/10.1021/acssuschemeng.0c07973.
19. Kulkarni, B.; Suvina, V.; Pramoda, K.; Balakrishna, R.G. Picomolar, Electrochemical Detection of Paraoxon Ethyl, by Strongly Coordinated NiCo2O4-SWCNT Composite as an Electrode Material. *J. Electroanal. Chem.* **2023**, *931*, 117175. https://doi.org/10.1016/j.jelechem.2023.117175.
20. Zak, J.; Kuwana, T. Electrooxidative catalysis using dispersed alumina on glassy carbon surfaces. *Am. Chem. Soc.* **1982**, *104*, 5514–5515. https://doi.org/10.1021/ja00384a056.
21. Lin, Q.; Li, Q.; Batchelor-McAuley, C.; Compton, R.G. Two-Electron, Two-Proton Oxidation of Catechol: Kinetics and Apparent Catalysis. *J. Phys. Chem. C* **2015**, *119*, 1489–1495. https://doi.org/10.1021/jp511414b.
22. Lima, A.P.; dos Santos, W.T.P.; Nossol, E.; Richter, E.M.; Munoz, R.A.A. Critical evaluation of voltammetric techniques for antioxidant capacity and activity: Presence of alumina on glassy-carbon electrodes alters the results. *Electrochim Acta* **2020**, *358*, 136925. https://doi.org/10.1016/j.electacta.2020.136925.
23. Novaković, T.; Barudžija, T.; Čomor, M.; Banković, P.; Mojović, Z. Electrochemical behavior of different types of alumina. *J. Electroanal. Chem.* **2021**, *895*, 115542. https://doi.org/10.1016/j.jelechem.2021.115542.
24. Ma, X.X.; He, X.Q. Electronically tailoring 3D flower-like graphene via alumina doping and incorporating Co as an efficient oxygen electrode catalyst in both alkaline and acid media. *J. Power Sources* **2017**, *353*, 28–39. https://doi.org/10.1016/j.jpowsour.2017.03.142.
25. Gu, W. Application of Nano-Alumina Electrodes in Electrochemical Sensing for Monitoring Exercise-Induced Lactate. *Int. J. Electrochem Sci.* **2025**, *20*, 101124. https://doi.org/10.1016/j.ijoes.2025.101124.
26. Jović-Jovičić, N.; Novaković, T.; Barudžija, T.; Ajduković, M.; Czerwinska, N.; Giosuè, C.; Mojović, Z. Sustainable Biochar–Alumina Composites for Electroanalytical Sensing of Herbicide and Antibiotic. *J. Xenobiotics* **2025**, *15*, 191. https://doi.org/10.3390/jox15060191.
27. Yoldas, B.E. Alumina gels that form porous transparent Al_2O_3. *J. Mater. Sci.* **1975**, *10*, 1856–1860. https://doi.org/10.1007/BF00754473.
28. Rouquerol, J.; Rouquerol, F.; Llewellyn, P.; Maurin, G.; Sing, K.S.W. *Adsorption by Powders and Porous Solids: Principle, Methodology and Applications*, 2nd ed.; Academic Press: New York, NY, USA, 2013.
29. Rouquerol, J.; Llewellyn, P.; Rouquerol, F. Is the Bet Equation Applicable to Microporous Adsorbents? In *Characterization of Porous Solids VII*. In *Studies in Surface Science and Catalysis*; Llewellyn, P.L., Rodriquez-Reinoso, F., Rouqerol, J., Seaton, N., Eds.; Elsevier Science: Amsterdam, The Netherlands, 2007; Volume 160, pp. 49–56.
30. Dubinin, M.M. Physical Adsorption of Gases and Vapors in Micropores. In *Progress in Surface and Membrane Science*; Cadenhead, D.A., Danielli, J.F., Rosenberg, M.D., Eds.; Academic Press: San Diego, CA, USA, 1975; Volume 9, pp. 1–70.

31. Barrett, E.P.; Joyner, L.G.; Halenda, P.P. The Determination of Pore Volume and Area Distributions in Porous Substances. I. Computations from Nitrogen Isotherms. *J. Am. Chem. Soc.* **1951**, *73*, 373–380.
32. Gholizadeh, Z.; Aliannezhadi, M. Tailoring the morphology and optical properties of alumina nanostructures by carbon quantum dot modification for enhanced heavy metal adsorption. *Microsyst. Nanoeng.* **2026**, *12*, 80. https://doi.org/10.1038/s41378-025-01134-8.
33. Baldovino-Medrano, V.G.; Niño-Celis, V.; Giraldo, R.I. Systematic Analysis of the Nitrogen Adsorption–Desorption Isotherms Recorded for a Series of Materials Based on Microporous–Mesoporous Amorphous Aluminosilicates Using Classical Methods. *J. Chem. Eng. Data* **2023**, *68*, 2512–2528. https://doi.org/10.1021/acs.jced.3c00257.
34. Desmurs, L.; Galarneau, A.; Cammarano, C.; Hulea, V.; Vaulot, C.; Nouali, H.; Lebeau, B.; Daou, T.J.; Soares, C.V.; Maurin, G.; et al. Determination of Microporous and Mesoporous Surface Areas and Volumes of Mesoporous Zeolites by Corrected *t*-Plot Analysis. *ChemNanoMat* **2022**, *8*, e202200051. https://doi.org/10.1002/cnma.202200051.
35. Nicholson, R.S. Theory and Application of Cyclic Voltammetry for Measurement of Electrode Reaction Kinetics. *Anal. Chem.* **1965**, *37*, 1351–1355. https://doi.org/10.1021/ac60230a016.
36. Lavagnini, I.; Antiochia, R.; Magno, F. An Extended Method for the Practical Evaluation of the Standard Rate Constant from Cyclic Voltammetric Data. *Electroanalysis* **2004**, *16*, 505–506. https://doi.org/10.1002/elan.200302851.
37. Bard, A.J.; Faulkner, L.R. *Electrochemical Methods: Fundamentals and Applications*, 2nd ed.; John Wiley & Sons: New York, NY, USA, 2001.
38. EFSA (European Food Safety Authority); Bellisai, G.; Bernasconi, G.; Carrasco Cabrera, L.; Castellan, I.; del Aguila, M.; Ferreira, L.; Greco, L.; Jarrah, S.; Leuschner, R.; et al. Modification of the existing maximum residue level for aclonifen in anise/aniseed. *EFSA J.* **2025**, *23*, e9514. https://doi.org/10.2903/j.efsa.2025.9514.
39. Edwards, F.L.; Tchounwou, P.B. Environmental Toxicology and Health Effects Associated with Methyl Parathion Exposure—A Scientific Review. *Int. J. Environ. Res. Public Health* **2005**, *2*, 430–441. https://doi.org/10.3390/ijerph2005030007.
40. Fronczak, M.; Károly, Z.; Banković, P.; Mojović, Z. The influence of precursor selection on electrochemical properties of radiofrequency thermal plasma synthesized graphene. *Microchem J.* **2024**, *199*, 110079. https://doi.org/10.1016/j.microc.2024.110079.
41. Guziejewski, D.; Smarzewska, S.; Skowron, M.; Ciesielski, W.; Nosal-Wiercińska, A.; Skrzypek, S. Rapid and Sensitive Voltammetric Determination of Aclonifen in Water Samples. *Acta Chim. Slov.* **2016**, *63*, 1–7. https://doi.org/10.17344/acsi.2014.583. PMID: 26970782.
42. dos Santos Caetano, K.; da Rosa, D.S.; Pizzolato, T.M.; dos Santos, P.A.M.; Hinrichs, R.; Benvenutti, E.V.; Dias, S.L.P.; Arenas, L.T.; Costa, T.M.H. MWCNT/zirconia porous composite applied as electrochemical sensor for determination of methyl parathion. *Micropor Mesopor Mat.* **2020**, *309*, 110583. https://doi.org/10.1016/j.micromeso.2020.110583.
43. Han, J.; Wu, T.; Li, F.; Zhao, M.; Liu, Y.; Guo, M.; Ran, Q.; Zhao, H. Highly sensitive methyl parathion electrochemical sensor designed from expired mung bean-derived porous carbon embellished with cerium oxide nanoparticles. *Microchem J.* **2024**, *201*, 110678. https://doi.org/10.1016/j.microc.2024.110678.
44. Ceylan, E.; Ozoglu, O.; Ipekci, H.H. Non-enzymatic detection of methyl parathion in water using CeO_2-CuO-decorated reduced graphene oxide. *Microchem J.* **2024**, *199*, 110261. https://doi.org/10.1016/j.microc.2024.110261.
45. Hou, X.; Liu, X.; Li, Z.; Zhang, J.; Du, G.; Ran, X.; Yang, L. Electrochemical determination of methyl parathion based on pillar[5]arene@AuNPs@reduced graphene oxide hybrid nanomaterials. *New J. Chem.* **2019**, *43*, 13048. https://doi.org/10.1039/c9nj02901j.
46. Mutharani, B.; Ranganathan, P.; Chen, S.-M.; Deepak Vishnu, S.K. Stimuli-enabled reversible switched aclonifen electrochemical sensor based on smart PNIPAM/PANI-Cu hybrid conducting microgel. *Sens. Actuators B Chem.* **2020**, *304*, 127232. https://doi.org/10.1016/j.snb.2019.127232.
47. Gopi, P.K.; Mutharani, B.; Chen, S.-M.; Chen, T.-W.; Eldesoky, G.E.; Ali, M.A.; Wabaidur, S.M.; Shaik, F.; Tzu, C.Y. Electrochemical sensing base for hazardous herbicide aclonifen using gadolinium niobate (GdNbO4) nanoparticles-actual river water and soil sample analysis. *Ecotoxicol. Environ. Saf.* **2021**, *207*, 111285. https://doi.org/10.1016/j.ecoenv.2020.111285.
48. Shetti, N.P.; Malode, S.J.; Vernekar, P.R.; Nayak, D.S.; Shetty, N.S.; Reddy, K.R.; Shukla, S.S.; Aminabhavi, T.M. Electro-sensing base for herbicide aclonifen at graphitic carbon nitride modified carbon electrode—Water and soil sample analysis. *Microchem J.* **2019**, *149*, 103976. https://doi.org/10.1016/j.microc.2019.103976.

Disclaimer/Publisher's Note: The statements, opinions and data contained in all publications are solely those of the individual author(s) and contributor(s) and not of MDPI and/or the editor(s). MDPI and/or the editor(s) disclaim responsibility for any injury to people or property resulting from any ideas, methods, instructions or products referred to in the content.